Home   Search   Collections   Journals   About   Contact us   My IOPscience

Picometer registration of zinc impurity states in $Bi_2Sr_2CaCu_2O_{8+}$ for phase determination in intra-unit-cell Fourier transform STM

Picometer registration of zinc impurity states in Bi$_2$Sr$_2$CaCu$_2$O$_{8+\delta}$ for phase determination in intra-unit-cell Fourier transform STM

M H Hamidian[1,2,8]**, I A Firmo**[1,2,8]**, K Fujita**[1,2,3]**,**
S Mukhopadhyay[1,2]**, J W Orenstein**[4]**, H Eisaki**[5]**, S Uchida**[3]**,**
M J Lawler[2]**, E-A Kim**[2] **and J C Davis**[1,2,6,7,9]

[1] CMPMS Department, Brookhaven National Laboratory, Upton, NY 11973, USA

[2] Laboratory of Solid State Physics, Department of Physics, Cornell University, Ithaca, NY 14853, USA

[3] Department of Physics, University of Tokyo, Bunkyo-ku, Tokyo 113-0033, Japan

[4] Department of Physics, University of California, Berkeley, CA 94720, USA

[5] Institute of Advanced Industrial Science and Technology, Tsukuba, Ibaraki 305-8568, Japan

[6] School of Physics and Astronomy, University of St Andrews, St Andrews, Fife KY16 9SS, UK

[7] Kavli Institute at Cornell for Nanoscale Science, Cornell University, Ithaca, NY 14853, USA

E-mail: jcdavis@ccmr.cornell.edu

Abstract. Direct visualization of electronic-structure symmetry within each crystalline unit cell is a new technique for complex electronic matter research (Lawler *et al* 2010 *Nature* **466** 347–51, Schmidt *et al* 2011 *New J. Phys.* **13** 065014, Fujita K *et al* 2012 *J. Phys. Soc. Japan* **81** 011005). By studying the Bragg peaks in Fourier transforms of electronic structure images and particularly by resolving both the real and imaginary components of the Bragg amplitudes, distinct types of intra-unit-cell symmetry breaking can be studied. However, establishing the precise symmetry point of each unit cell in real space is crucial

[8] These authors contributed equally to this paper.

[9] Author to whom any correspondence should be addressed.

in defining the phase for such a Bragg-peak Fourier analysis. Exemplary of this challenge is the high-temperature superconductor $Bi_2Sr_2CaCu_2O_{8+\delta}$ for which the surface Bi atom locations are observable, while it is the invisible Cu atoms that define the relevant CuO_2 unit-cell symmetry point. Here we demonstrate, by imaging with picometer precision the electronic impurity states at individual Zn atoms substituted at Cu sites, that the phase established using the Bi lattice produces a $\sim 2\%(2\pi)$ error relative to the actual Cu lattice. Such a phase assignment error would not diminish reliability in the determination of intra-unit-cell rotational symmetry breaking at the CuO_2 plane (Lawler *et al* 2010 *Nature* **466** 347–51, Schmidt *et al* 2011 *New J. Phys.* **13** 065014, Fujita K *et al* 2012 *J. Phys. Soc. Japan* **81** 011005). Moreover, this type of impurity atom substitution at the relevant symmetry site can be of general utility in phase determination for the Bragg-peak Fourier analysis of intra-unit-cell symmetry.

S Online supplementary data available from stacks.iop.org/NJP/14/053017/mmedia

Contents

1. Spectroscopic imaging scanning tunneling microscopy and its Bragg-peak Fourier analysis

In spectroscopic imaging scanning tunneling microscopy (SI-STM), the differential tunneling conductance $dI/dV(r, V) \equiv g(r, V)$ between the tip and sample is measured as a function of both the location r and the electron energy $E = eV$. For a simple metal, $g(r, V) = LDOS(r, E = eV$ where $LDOS(r, E)$ is the spatially and energy-resolved local-density-of-electronic states [4]. This direct assignment cannot be made for materials whose electronic structure is strongly heterogeneous at the nanoscale [5, 6]. However, even in those circumstances distances (wavelengths) and spatial symmetries in the $g(r, V)$ images should retain their physical significance. SI-STM has proven to be of wide utility and growing significance in electronic structure studies, especially in situations where the translationally invariant non-interacting single-particle picture does not hold [6–14].

A key practical challenge for all such SI-STM studies is that, over the week(s) of continuous data acquisition required to measure a $g(r, V)$ dataset having both $\geqslant 50$ pixels within each crystal unit cell and the large field of view (FOV) required for precision Fourier analysis, thermal and mechanical drifts distort the $g(r, V)$ images subtly. Such $g(r, V)$ distortions, while pervasive, are usually imperceptible in conventional analyses. However, they strongly impact on the capability to determine intra-unit-cell symmetry breaking, because the perfect lattice-periodicity throughout $g(r, V)$ that is necessary for Bragg-peak Fourier analysis is disrupted [1].

To address this issue, we recently introduced a post-measurement distortion correction technique that is closely related to an approach we developed earlier to address incommensurate crystal modulation effects [15]. The new procedure [1–3, 16] identifies a slowly varying field $u(r)$ [17] that measures the displacement vector u of each location r in a topographic image of the crystal surface $T(r)$, from the location $r - u(r)$ where it should be if $T(r)$ were perfectly periodic with the symmetry and dimensions established by x-ray or other scattering studies of the same material.

To understand the procedure, consider an atomically resolved topograph $T(r)$ with tetragonal symmetry. In SI-STM, the $T(r)$ and its simultaneously measured $g(r, V)$ are specified by measurements on a square array of pixels with coordinates labeled $r = (x, y)$. The power-spectral-density (PSD) Fourier transform of $T(r)$, $|\tilde{T}(q)|^2$, where $\tilde{T}(q) = \mathrm{Re}\,\tilde{T}(q) + i\mathrm{Im}\,\tilde{T}(q)$, then exhibits two distinct peaks representing the atomic corrugations. These are centered at the first reciprocal unit cell Bragg wavevectors $Q_a = (Q_{ax}, Q_{ay})$ and $Q_b = (Q_{bx}, Q_{by})$ with a and b being the unit cell vectors. Next, we apply a computational 'lock-in' technique in which $T(r)$ is multiplied by reference cosine and sine functions with periodicity set by the wavevectors Q_a and Q_b and whose origin is chosen at an apparent atomic location in $T(r)$. The resulting four images are filtered to retain only the q-space regions within a radius $\delta q = \frac{1}{\lambda}$ of the four Bragg peaks; the magnitude of λ is chosen to capture only the relevant image distortions (in particular, δq is chosen here to be smaller than the $Bi_2Sr_2CaCu_2O_{8+\delta}$ supermodulation wavevector). This procedure results in retaining the local phase information $\theta_a(r), \theta_b(r)$ that quantifies the local displacements from perfect periodicity:

$$X_a(r) = \cos\theta_a(r), \quad Y_a(r) = \sin\theta_a(r), \tag{1a}$$

$$X_b(r) = \cos\theta_b(r), \quad Y_b(r) = \sin\theta_b(r). \tag{1b}$$

Dividing the appropriate pairs of images then allows one to extract

$$\theta_a(r) = \tan^{-1}\frac{Y_a(r)}{X_a(r)}, \tag{2a}$$

$$\theta_b(r) = \tan^{-1}\frac{Y_b(r)}{X_b(r)}. \tag{2b}$$

Of course, in a perfect lattice $\theta_a(r), \theta_b(r)$ would be independent of r. However, in the real image $T(r)$, $u(r)$ represents the distortion of the local maxima away from their expected perfectly periodic locations, with an identical distortion occurring in the simultaneous spectroscopic data $g(r, V)$. Considering only the components periodic with the lattice, the measured topograph can therefore be represented by

$$T(r) = T_0\left[\cos\left(Q_a \cdot (r + u(r))\right) + \cos\left(Q_b \cdot (r + u(r))\right)\right]. \tag{3}$$

Correcting this for the spatially dependent phases $\theta_a(\boldsymbol{r})$, $\theta_b(\boldsymbol{r})$ generated by $\boldsymbol{u}(\boldsymbol{r})$ requires an affine transformation at each point in (x, y) space. From equation (3) we see that the actual local phase of each cosine component at a given spatial point $\boldsymbol{r}$, $\varphi_a(\boldsymbol{r})$, $\varphi_b(\boldsymbol{r})$, can be written as

$$\varphi_a(\boldsymbol{r}) = \boldsymbol{Q}_a \cdot \boldsymbol{r} + \theta_a(\boldsymbol{r}), \tag{4a}$$

$$\varphi_b(\boldsymbol{r}) = \boldsymbol{Q}_b \cdot \boldsymbol{r} + \theta_b(\boldsymbol{r}), \tag{4b}$$

where $\theta_i(\boldsymbol{r}) = \boldsymbol{Q}_i \cdot \boldsymbol{u}(\boldsymbol{r})$, $i = a, b$, is the additional phase generated by the distortion field $\boldsymbol{u}(\boldsymbol{r})$. This simplifies equation (2) to

$$T(\boldsymbol{r}) = T_0 \left[\cos(\varphi_a(\boldsymbol{r})) + \cos(\varphi_b(\boldsymbol{r})) \right], \tag{5}$$

which is defined in terms of its local phase fields only, and every peak associated with an atomic local maximum in the topographic image has the same φ_a and φ_b. The goal is then to find a transformation, using the given phase information $\varphi_{a,b}(\boldsymbol{r})$, to map the distorted lattice onto a perfectly periodic one. This is equivalent to finding a set of local transformations that makes $\theta_{a,b}$ take on constant values, $\bar{\theta}_a$ and $\bar{\theta}_b$, over all space. Thus, let $\boldsymbol{r}$ be a point on the unprocessed (distorted) $T(\boldsymbol{r})$, and let $\tilde{\boldsymbol{r}} = \boldsymbol{r} - \boldsymbol{u}(\boldsymbol{r})$ be the point of equal phase on the 'perfectly' lattice-periodic image that needs to be determined. This produces a set of equivalence relations

$$\begin{aligned} \boldsymbol{Q}_a \cdot \boldsymbol{r} + \theta_a(\boldsymbol{r}) &= \boldsymbol{Q}_a \cdot \tilde{\boldsymbol{r}} + \bar{\theta}_a \\ \boldsymbol{Q}_b \cdot \boldsymbol{r} + \theta_b(\boldsymbol{r}) &= \boldsymbol{Q}_b \cdot \tilde{\boldsymbol{r}} + \bar{\theta}_b \end{aligned} \tag{6}$$

Solving for the components of $\tilde{\boldsymbol{r}}$ and then re-assigning the $T(\boldsymbol{r})$ values measured at $\boldsymbol{r}$ to the new location $\tilde{\boldsymbol{r}}$ in the (x, y) coordinates produces a topograph with 'perfect' lattice periodicity. To solve for $\tilde{\boldsymbol{r}}$ we rewrite equation (6) in matrix form:

$$\boldsymbol{Q} \begin{pmatrix} \tilde{r}_1 \\ \tilde{r}_2 \end{pmatrix} = \boldsymbol{Q} \begin{pmatrix} r_1 \\ r_2 \end{pmatrix} - \boldsymbol{Q} \begin{pmatrix} \bar{\theta}_a - \theta_a(\boldsymbol{r}) \\ \bar{\theta}_b - \theta_b(\boldsymbol{r}) \end{pmatrix}, \tag{7}$$

where

$$\boldsymbol{Q} = \begin{pmatrix} Q_{ax} & Q_{ay} \\ Q_{bx} & Q_{by} \end{pmatrix}. \tag{8}$$

Because $\boldsymbol{Q}_a$ and $\boldsymbol{Q}_b$ are orthogonal, $\boldsymbol{Q}$ is invertible allowing one to solve for the displacement field $\boldsymbol{u}(\boldsymbol{r})$ which maps $\boldsymbol{r}$ to $\tilde{\boldsymbol{r}}$ as

$$\boldsymbol{u}(\boldsymbol{r}) = \boldsymbol{Q}^{-1} \begin{pmatrix} \bar{\theta}_a - \theta_a(\boldsymbol{r}) \\ \bar{\theta}_b - \theta_b(\boldsymbol{r}) \end{pmatrix}, \tag{9}$$

In practice, we use the convention $\bar{\theta}_i = 0$, which generates a 'perfect' lattice with an atomic peak at the origin; this is equivalent to ensuring that there are no imaginary (sine) components to the Bragg peaks in the Fourier transform.

Using this technique, one can estimate $\boldsymbol{u}(\boldsymbol{r})$ and thereby undo distortions in the raw $T(\boldsymbol{r})$ data with the result that it is transformed into a distortion-corrected topograph $T'(\boldsymbol{r})$ exhibiting the known periodicity and symmetry of the termination layer of the crystal. The key step for electronic-structure symmetry determination is then that the identical geometrical transformations to undo $\boldsymbol{u}(\boldsymbol{r})$ in $T(\boldsymbol{r})$ yielding $T'(\boldsymbol{r})$ are also carried out on every $g(\boldsymbol{r}, V)$ acquired simultaneously with the $T(\boldsymbol{r})$ to yield a distortion-corrected $g'(\boldsymbol{r}, V)$. The $T'(\boldsymbol{r})$ and $g'(\boldsymbol{r}, V)$ are then registered to each other and to the lattice with excellent precision. This procedure can be used quite generally with SI-STM data that exhibit appropriately high resolution in both $\boldsymbol{r}$-space and $\boldsymbol{q}$-space.

2. 'Real' and 'imaginary' contributions to the Bragg peaks in $\tilde{g}(q, V)$

Bragg-peak Fourier analysis of an electronic structure image $g(r, V)$ focuses upon $\tilde{g}(q, V) =$ Re $\tilde{g}(q, V) + \mathrm{i}\,\mathrm{Im}\,\tilde{g}(q, V)$, its complex valued two-dimensional (2D) Fourier transform. Here Re $\tilde{g}(q, V)$ is the cosine and Im $\tilde{g}(q, V)$ the sine Fourier component, respectively. By focusing on the Bragg peaks $q = Q_a$, Q_b only those electronic phenomena with the same spatial periodicity as the crystal are considered. Obviously, successful application of this approach when using $g(r, V)$ images requires: (i) highly accurate registry of the unit-cell origin to satisfy the extreme sensitivity in $\tilde{g}(q, V)$ to the phase, (ii) that the $g(r, V)$ data set has adequate sub-unit-cell resolution without which the distinction between the four inequivalent Bragg amplitudes at Q_a, Q_b would be zero and (iii) that this same $g(r, V)$ be measured in a large FOV so as to achieve high resolution in q-space. Only recently has this combination of characteristics in $g(r, V)$ measurement been achieved [1–3].

With the availability of such data, several measures of intra-unit-cell breaking of crystal symmetry by the electronic structure become possible from the study of the real and imaginary components of the Bragg amplitudes in $\tilde{g}(Q, V)$. For example, if the crystal unit cell is tetragonal with 90°-rotational (C_{4v}) symmetry, one can search for intra-unit-cell 'nematicity' (breaking of C_{4v} down to 180°-rotational (C_{2v}) symmetry) in the electronic structure by considering $O_N(V) = \mathrm{Re}\,\tilde{g}(Q_b, V) - \mathrm{Re}\,\tilde{g}(Q_a, V)$ [1–3]. Similarly, if the crystal unit-cell is centrosymmetric, one can search for intra-unit-cell breaking of inversion symmetry in electronic structure using $O_I(V) = |\mathrm{Im}\,\tilde{g}(Q_a, V)| + |\mathrm{Im}\,\tilde{g}(Q_b, V)|$. Obviously, however, in both of these cases and in general, the correct determination of Re $\tilde{g}(q, V)$ and Im $\tilde{g}(q, V)$ is critical. The assignment of the zero of coordinates at the symmetry point of the unit-cell (and thus the correct choice of phase) is therefore the fundamental practical challenge of Bragg-peak Fourier transform SI-STM.

3. Intra-unit-cell electronic symmetry breaking in Bi$_2$Sr$_2$CaCu$_2$O$_{8+\delta}$

An excellent example of this challenge can be found in the copper-oxide high-temperature superconductor $Bi_2Sr_2CaCu_2O_{8+\delta}$. In general, copper-oxide superconductors are 'charge-transfer' Mott insulators and are strongly antiferromagnetic due to inter-copper superexchange [18]. Doping these materials with a hole density p to create superconductivity is achieved by removing electrons from the O atoms in the CuO_2 plane [19, 20]. Antiferromagnetism exists for $p < 2$–5%, superconductivity occurs in the range 5–10% $< p <$ 25–30%, and a Fermi liquid state appears for $p > 25$–30%. For $p < 20$% an unusual electronic excitation with energy scale $|E| = \Delta_1$, which is anisotropic in k-space [21–25], appears at temperatures far above the superconducting critical temperature. This region of the phase diagram has been labeled the 'pseudogap' (PG) phase because the energy scale Δ_1 could be the energy gap of a distinct electronic phase [21, 22].

Intra-unit-cell spatial symmetries of the $E \sim \Delta_1$ (PG) states can be imaged directly using SI-STM in underdoped cuprates [1–3, 6, 16]. Typically, the function $Z(r, V) = g(r, +V)/g(r, -V)$ is used because it eliminates the severe systematic errors in $g(r, V)$ generated by the intense electronic heterogeneity effects specific to these materials [1–3, 5, 6, 11, 16]. These $Z(r, E)$ images reveal compelling evidence for intra-unit-cell C_{4v} symmetry breaking specific to the states at the $E \sim \Delta_1$ pseudogap energy [6]. However, for Bragg-peak Fourier transform studies of this effect the choice of origin of the CuO_2 unit cell (and thus the

phase of the Fourier transforms) was determined by using the imaged locations of the Bi atoms in the BiO layer [1–3], while it is knowledge of the actual Cu atom locations that is required to most confidently examine intra-unit-cell symmetry breaking of the CuO_2 unit cell.

4. Cu-lattice phase-resolution challenge in $Bi_2Sr_2CaCu_2O_{8+\delta}$

To identify these sites and thus the correct phase, we studied lightly Zn-doped $Bi_2Sr_2CaCu_2O_{8+\delta}$ crystals with $p \sim 20\%$. Each $g(r, E = \text{eV})$ map required ~ 5 days and a typical resulting topograph $T(r)$ with 64 pixels covering the area of each CuO_2 unit cell is shown in figure 1(a). This is an unprocessed topographic image $T(r)$ of the BiO layer with the bright dots occurring at the location of Bi atoms. The inset shows a tightly focused measurement at the location of one of the Bragg peaks in $|\tilde{T}(q)|^2$; this clearly has spectral weight distributed over numerous pixels indicating the imperfect nature of the periodicity in this $T(r)$. Figure 1(b) is the simultaneously measured image of electronic structure $g(r, E)$ determined near $E \sim \Delta_1$. Figure 1(c) shows the PSD Fourier transform of figure 1(b), while its inset focuses upon a single Bragg peak. Figure 1(d) shows the processed topographic image $T'(r)$ after distortion correction using equation (9). The subtlety of these corrections is such that figure 1(d) appears virtually identical to figure 1(a) at first sight. However, the inset shows that the Bragg peak of the PSD Fourier transform $|\tilde{T}(q)|^2$ of figure 1(d) now becomes isotropic and consists of just a single pixel; this indicates that Bi atom periodicity is now as perfect as possible given the limitations of q-space resolution from the finite FOV. Figure 1(e) is the $g(r, V)$ data of figure 1(b), but now processed in the same distortion correction fashion as figure 1(d) to yield a function $g'(r, V)$. Its PSD Fourier transform $|\tilde{g}'(q, V)|^2$ as shown in figure 1(f) reveals how the Bragg peaks are now also sharp, indicating that the same spatial periodicity now exists in the electronic structure images (inset of figure 1(e)). Nevertheless, the location of the Cu sites in the CuO_2 plane cannot be determined from the BiO $T'(r)$ and therefore the phase for Bragg-peak Fourier analysis of $\tilde{g}'(q, V)$ from the CuO_2 plane retains some ambiguity.

5. Imaging the electronic impurity state at Zn atoms substituted for Cu

To directly identify the symmetry point of the CuO_2 unit cell in a BiO topograph, we image $g(r, V = -1.5\,\text{mV})$ measured on Zn-doped $Bi_2Sr_2CaCu_2O_{8+\delta}$ crystals. A conductance map in a 60 nm square region (simultaneous topograph figure 2(a)) is shown in figure 2(b); the overall light background is indicative of a very low conductance near E_F as expected in the superconducting state. However, we also detect a significant number of randomly distributed dark sites corresponding to areas of high conductance each with a distinct fourfold symmetric shape and the same relative orientation. The spectrum at the center of a dark site has a very strong intra-gap conductance peak at energy $E = -1.5 \pm 0.5\,\text{meV}$, while the superconducting coherence peaks are suppressed [26]. This is a unitary strength quasiparticle scattering resonance at a single, potential-scattering, impurity atom in a d-wave superconductor [26, 27]. These signatures can be used to identify the location of Zn atoms substituted on the Cu sites of $Bi_2Sr_2CaCu_2O_{8+\delta}$.

Figure 2(a) actually shows the topographic image $T'(r)$ of the BiO layer *after* its distortion correction has been carried out, whereas figure 2(b) shows the identically distortion-corrected image of differential conductance. Fourteen Zn impurity state sites at Cu sites in the CuO_2 plane are observed. Imaging the locations of these individual Zn resonance sites with approximately
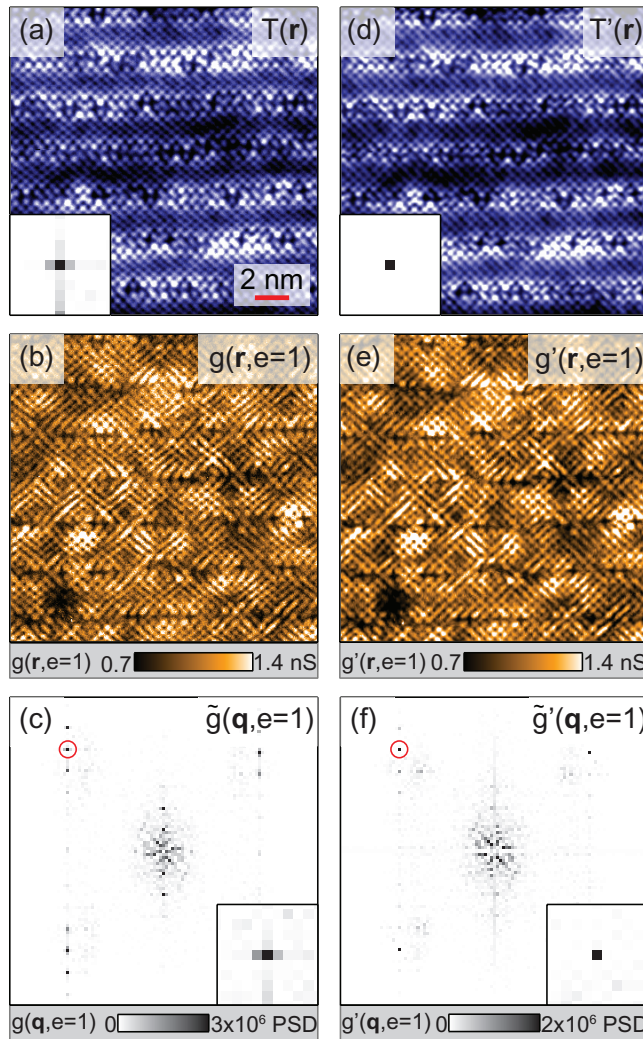
Figure 1. (a) Raw topographic image $T(\mathbf{r})$ of the BiO layer of Bi$_2$Sr$_2$CaCu$_2$O$_{8+\delta}$ in a 20 nm FOV. The inset shows one of the Bragg peaks. All the data in this figure were acquired at 1 GΩ junction resistance, −110 mV tip–sample bias. (b) Unprocessed differential conductance image $g(\mathbf{r}, E/\Delta_1(\mathbf{r}) = 1)$ at the superconducting coherence peak energy. This image has been measured in the same FOV as (a). (c) PSD Fourier transform of (b), $|\tilde{g}(\mathbf{q}, e = 1)|^2$. The inset shows the same Bragg peak as (a). The red circle indicates the location of the Bragg peak shown in the insets of figures 1(a)–(f). (d) The same topographic image $T'(\mathbf{r})$ as in (a), but after applying the distortion correction algorithm. The inset shows one of the resulting isotropic Bragg peaks confined in a single pixel (the same as in (a)). (e) The same differential conductance data $g'(\mathbf{r}, e = 1)$ as in (b) after applying the distortion correction algorithm. (f) PSD Fourier transform of (e), $|\tilde{g}'(\mathbf{q}, e = 1)|^2$. The red circle indicates the location of the Bragg peak shown in the insets of figures 1(a)–(f).

picometer resolution allows precision identification of the symmetry point of each CuO$_2$ unit cell and an excellent estimate of the correct phase required for Bragg-peak Fourier analysis of the CuO$_2$ plane electronic structure.
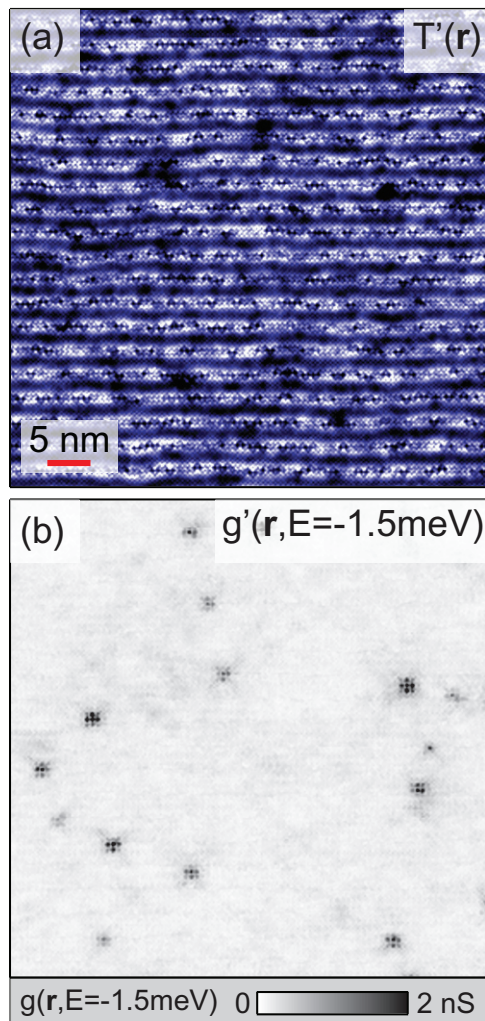
Figure 2. (a) A $\sim$60 nm square FOV $T'(\boldsymbol{r})$. The data shown in this image have been processed using the distortion correction algorithm. (b) Simultaneously measured $g'(\boldsymbol{r}, V = -1.5\,\text{mV})$ in the same FOV as (a). Fourteen Zn impurity resonances are distinguishable in this image. These data have been processed using the distortion correction algorithm. The data in (a) and (b) were acquired at 1 GΩ junction resistance, 60 mV tip–sample bias.

6. Determination of Cu-lattice phase error from Bi-lattice calibration

In figure 3, each pair of panels (a–b), (c–d), ..., (w–x) contains the simultaneously measured and identically distortion-corrected images $T'(\boldsymbol{r})$ and $g'(\boldsymbol{r}, -1.5\,\text{mV})$, each with 76 pixels inside the area of every CuO$_2$ unit cell. The coordinates of every Bi atom in the perfectly square lattice are known with approximately picometer precision in these $T'(\boldsymbol{r})$ images. The location of the Zn impurity state in each of the $g'(\boldsymbol{r}, -1.5\,\text{mV})$ images is determined by fitting a 2D Gaussian to the central peak of the Zn resonance; a typical resulting error bar for the location of the maximum is a value between 1 and 2 pm (see supplementary information, section I, available from stacks.iop.org/NJP/14/053017/mmedia). The smallness of this error with respect to the
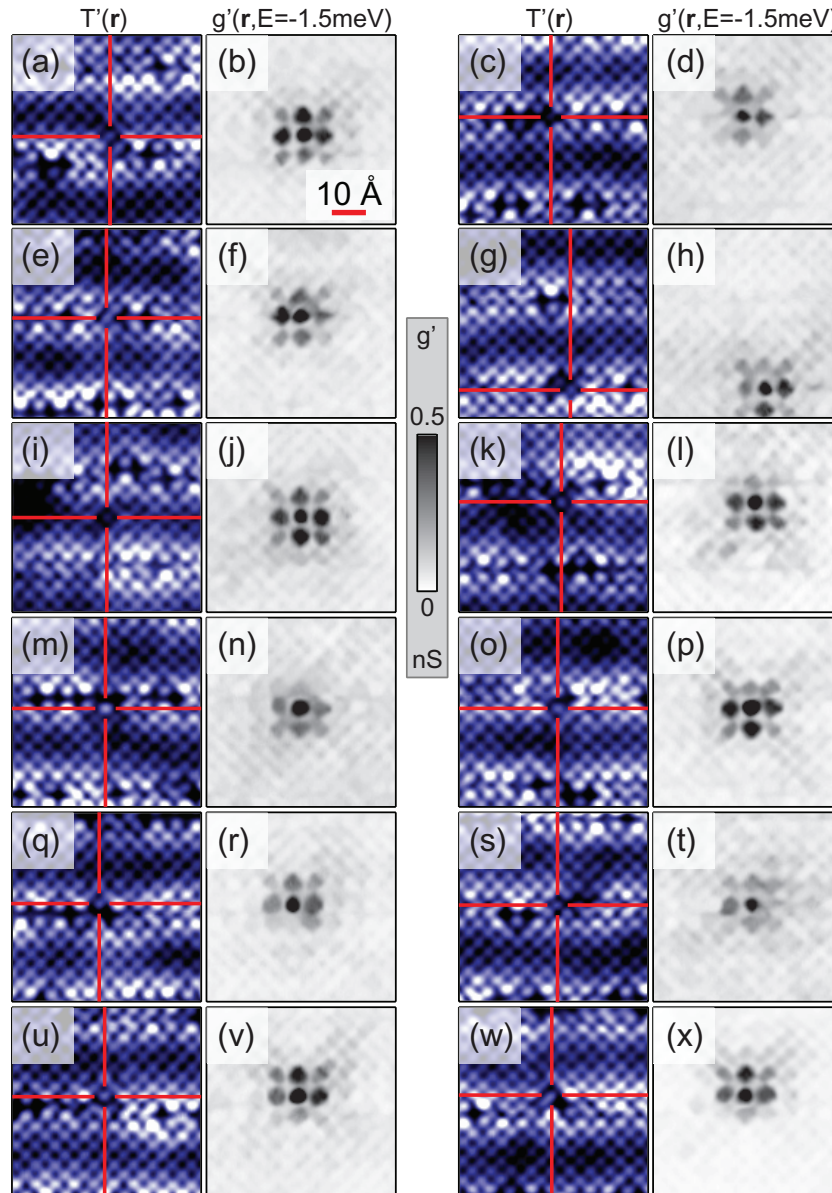
Figure 3. (a, b) Simultaneous $T'(\mathbf{r})$ image of a 60 Å FOV containing one Zn atom. The red cross indicates the Bi atom nearest to the Zn atom shown in $g'(\mathbf{r}, e\text{V})$ from (b). The data in (a) and (b) were acquired at $1\,\text{G}\Omega$ junction resistance, 60 mV, and were obtained from a double-layer $g(\mathbf{r}, E)$ map. A total time of 340 ms has elapsed between the measurement of (a) and (b). All subsequent image pairs represent equivalent data at a different location. All data in this figure were obtained from five maps with identical acquisition parameters, and have been processed using the distortion correction algorithm.

pixel size is well understood in terms of the large signal-to-noise ratio at Zn resonances [26] (supplementary information, section I). These procedures yield the displacement vector $\boldsymbol{d}$ of every Zn-resonance maximum from the site of the nearest Bi atom as identified in $T'(\mathbf{r})$.
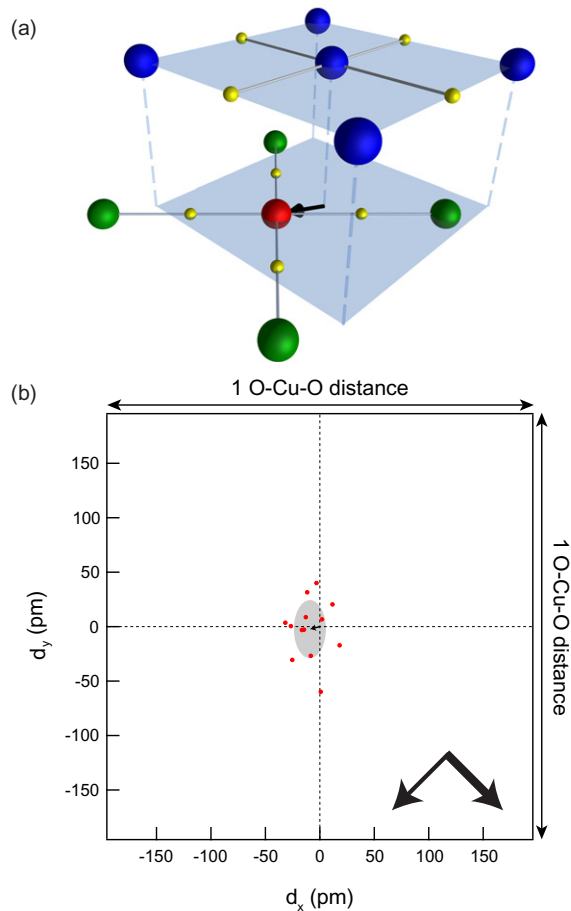
Figure 4. (a) Schematic relationship between Bi atom locations in $T'(\boldsymbol{r})$ and the Cu sites at the symmetry point of the CuO_2 unit cell. The Bi (blue) atoms are directly above the Cu (green) atoms; in between the two atoms, there is an oxygen atom (not shown here). Sometimes, a Zn impurity atom (red) is found at one of the Cu sites. Vector **d** is non-zero when there is a small shift in the XY-plane between the positions of a Cu (or Zn impurity) atom and the Bi atom directly above it. (b) Displacement vector between the center point of each Zn resonance in $g'(\boldsymbol{r}, \text{eV})$ and the nearest Bi atom in $T'(\boldsymbol{r})$ (see figure 3). The average displacement vector over all the (Zn, Bi) XY-plane distances is shown as a black arrow. The ellipse about the average displacement arrow corresponds to 1 standard deviation of the average displacement. The individual (Zn, Bi) XY-plane displacement data are shown by red dots. The fast and slow scan directions are, respectively, indicated by the thicker and thinner arrows at the bottom right corner of this figure.

Figure 4(a) indicates using a black arrow the displacement vector $\boldsymbol{d}$ between the Bi atom (top) and Cu atom (bottom) if a rigid xy-displacement existed between them. The blue planes indicate the relative positions of the two layers if there were no such shift and thus $\boldsymbol{d} = 0$. Figure 4(b) shows a combined analysis of the measured values of $\boldsymbol{d}$ for all the CuO_2 unit cells

containing a Zn atom (with the origin of each centered at the relevant Bi atom identified from the nearest maximum in $T'(r)$ images in figure 3). The measured d of every Zn resonance is shown as a red dot. The resulting average (Zn, Bi) displacement vector shown in black has a magnitude of $\sim 2\%$ of the CuO_2 unit cell dimension (1 standard deviation of the distribution is indicated by the grey ellipse). It is quite obvious from figure 4(b) that the Zn resonances are extremely close to the Bi sites, meaning that the CuO_2 layer is not shifted significantly from its expected location below the BiO layer (figure 4(a)).

Beyond the fact that the average displacement $\langle d \rangle$ represents only a $\sim 2\%(2\pi)$ error in the phase determination for the CuO_2 layer when using the BiO layer, other information on systematic errors within the SI-STM approach can be examined using these data. For example, the observed distribution of d rules out the existence of any discrete pixel displacement between $T(r)$ and its simultaneously measured $g(r, V)$, as might occur if there were a software or processing error. Another point is that any spatial drift of the tip location during the hundreds of elapsed milliseconds between the measurement of the topographic signal and the differential conductance signal is also below 2% of the unit cell dimension. In fact the data in Figures 2–4 show that, for our instruments, the measured $T(r)$ and $g(r, V = -1.5\,\mathrm{mV})$ are registered to each other within a few pm. Additionally, studies of this same set of Zn resonances using the 180°-rotated scan direction (supplementary information, section II) yield an equivalently narrow (but distinct) distribution of values of d. Moreover, the center of this distribution is not shifted along the scan relative to that in figure 4(b), indicating that random picometer scale image distortions dominate the d distribution and not the trajectory of the tip. Thus, we do not currently regard the apparent displacement (CuO_2, BiO) in figure 4(b) as a property of the crystal lattice, but rather due to measurement limitations at these picometer length scales (see supplementary information, section II).

7. Conclusions and future

Three key practical conclusions emerge from these studies. Firstly, the lateral shift between the surface BiO layer and the CuO_2 layer is measured at less than 2% of the unit cell dimension. Secondly, at this approximately picometer precision there is no resolvable spatial drift of the tip location during the fractions of a second between the measurement of the topographic signal and the differential conductance signal. Perhaps most importantly, the $\sim 2\%(2\pi)$ phase error in the choice of the Cu-lattice origin observed here would not, based on results from our simulations (supplementary information, section III, available from stacks.iop.org/NJP/14/053017/mmedia), impact on Fourier transform analysis using $\mathrm{Re}\,\tilde{g}(Q_a, V)$ and $\mathrm{Re}\,\tilde{g}(Q_b, V)$ to determine symmetry breaking in $g(r, V)$. However, such a $\sim 2\%(2\pi)$ phase error would have a significant effect on the measure of intra-unit-cell inversion-symmetry breaking like $O_I(V)$, yielding an incorrect non-zero value for $\mathrm{Im}\,\tilde{g}(Q_a, V)$ or $\mathrm{Im}\,\tilde{g}(Q_b, V)$ of $\sim 15\%$ of $\mathrm{Re}\,\tilde{g}(Q_a, V)$ or $\mathrm{Re}\,\tilde{g}(Q_b, V)$ (supplementary information, section III). Specifically, a $\sim 2\%(2\pi)$ phase assignment error for the Cu sites does not diminish the reliability in the determination of intra-unit-cell rotational symmetry breaking at the CuO_2 plane [1–3]. Of more long-term significance is the fact that impurity atom substitution at the relevant symmetry site as demonstrated here can be of general utility in accurate phase determination for Bragg-peak Fourier analysis of intra-unit-cell symmetry.

Acknowledgments

References

[1] Lawler M J *et al* 2010 Intra-unit-cell electronic nematicity of the high-T_c copper-oxide pseudogap states *Nature* **466** 347–51

[2] Schmidt A R *et al* 2011 Electronic structure of the cuprate superconducting and pseudogap phases from spectroscopic imaging STM *New J. Phys.* **13** 065014

[3] Fujita K *et al* 2012 Spectroscopic imaging STM studies of electronic structure in the superconducting and pseudogap phases of cuprate high-T_c superconductors *J. Phys. Soc. Japan* **81** 011005

[4] Wiesendanger R 1998 *Scanning Tunneling Spectroscopy: Methods and Applications* (Cambridge: Cambridge University Press) pp 109–14

[5] Hanaguri T *et al* 2007 Quasiparticle interference and superconducting gap in $Ca_{2-x}Na_xCuO_2Cl_2$ *Nature Phys.* **3** 865–71

[6] Kohsaka Y *et al* 2007 An intrinsic bond-centered electronic glass with unidirectional domains in underdoped cuprates *Science* **315** 1380–85

[7] Gomes K K *et al* 2007 Visualizing pair formation on the atomic scale in the high-T_c superconductor $Bi_2Sr_2CaCu_2O_{8+\delta}$ *Nature* **447** 569–72

[8] Boyer M C *et al* 2007 Imaging the two gaps of the high-temperature superconductor $Bi_2Sr_2CuO_{6+x}$ *Nat. Phys.* **3** 802–6

[9] Niestemski F C *et al* 2007 A distinct bosonic mode in an electron-doped high-transition-temperature superconductor *Nature* **450** 1058–61

[10] Yin Y *et al* 2009 Scanning tunneling spectroscopy and vortex imaging in the iron pnictide superconductor $BaFe_{1.8}Co_{0.2}As_2$ *Phys. Rev. Lett.* **102** 097002

[11] Massee F *et al* 2010 Pseudogap-less high T_c superconductivity in $BaCo_xFe_{2-x}As_2$ *Eur. Phys. Lett.* **92** 57012

[12] Allan M P *et al* 2011 private communication

[13] Schmidt A R *et al* 2010 Imaging the Fano lattice to 'hidden order' transition in URu_2Si_2 *Nature* **465** 570–6

[14] Hamidian M *et al* 2011 How Kondo-holes create intense nanoscale heavy-fermion hybridization disorder *Proc. Natl Acad. Sci. USA* **108** 18233–7

[15] Slezak J A *et al* 2008 Imaging the impact on cuprate superconductivity of varying the interatomic distances within individual crystal unit cells *Proc. Natl Acad. Sci. USA* **105** 3203–8

[16] Mesaros A *et al* 2011 Topological defects coupling smectic modulations to intra-unit-cell nematicity in cuprates *Science* **333** 426–30

[17] Chaikin P M and Lubensky T C 2010 *Principles of Condensed Matter Physics* (Cambridge: Cambridge University Press) pp 330–2

[18] Anderson P W 1987 The resonating valence bond state in La_2CuO_4 *Science* **235** 1196–8

[19] Chen C T *et al* 1991 Electronic states in $La_{2-x}Sr_xCuO_{4-\delta}$ probed by soft-x-ray absorption *Phys. Rev. Lett.* **66** 104

IOP Institute of Physics **ΦDEUTSCHE PHYSIKALISCHE GESELLSCHAFT**

[20] Sakurai Y *et al* 2011 Imaging doped holes in a cuprate superconductor with high-resolution Compton scattering *Science* **332** 698–702

[21] Timusk T and Statt B 1999 The pseudogap in high-temperature superconductors: an experimental survey *Rep. Prog. Phys.* **62** 61

[22] Hüefner S, Hossain M A, Damascelli A and Sawatzky G A 2008 Two gaps make a high-temperature superconductor *Rep. Prog. Phys.* **71** 062501

[23] Damascelli A, Hussain Z and Shen Z-X 2003 Angle-resolved photoemission studies of the cuprate superconductors *Rev. Mod. Phys.* **75** 473

[24] Campuzano J C, Norman M R and Randeria M 2004 *The Physics of Superconductors* vol II, ed K H Bennemann and J B Ketterson (New York: Springer) pp 167–273

[25] Norman M R and Pépin C 2003 The electronic nature of high temperature cuprate superconductors *Rep. Prog. Phys.* **66** 1547

[26] Pan S H *et al* 2000 Imaging the effects of individual zinc impurity atoms on superconductivity in $Bi_2Sr_2CaCu_2O_{8+\delta}$ *Nature* **403** 746–50

[27] Balatsky A V *et al* 2006 Impurity-induced states in conventional and unconventional superconductors *Rev. Mod. Phys.* **78** 373–433